Densification behavior and microstructure evolution of yttrium-doped ThO_2 ceramics

Y. Cherkaski, Nicolas Clavier, L. Brissonneau, Renaud Podor, N. Dacheux

Densification behavior and microstructure evolution of yttrium-doped ThO_2 ceramics

Y. Cherkaski [1,2], N. Clavier [2,], L. Brissonneau [1], R. Podor [2], N. Dacheux [2]*

[1] CEA/DEN/DTN/SMTA/LIPC, Site de Cadarache, 13108 St-Paul lez Durance, France
[2] ICSM – UMR 5257, CEA/CNRS/ENSCM/Univ. Montpellier, Site de Marcoule, BP 17171, 30207 Bagnols/Cèze cedex, France

*** Corresponding author :**

Dr. Nicolas CLAVIER
ICSM – UMR 5257 CEA/CNRS/UM/ENSCM
Site de Marcoule – Bât 426
BP 17171
30207 Bagnols sur Cèze
France

Phone : + 33 4 66 33 92 08
Fax : + 33 4 66 79 76 11

nicolas.clavier@icsm.fr

Abstract :

Sintering of $Th_{1-x}Y_xO_{2-x/2}$ ceramics (x = 0.01, 0.08, 0.15 and 0.22), planned to be used as solid electrolytes in oxygen sensors for sodium-cooled fast nuclear reactors, was investigated. High densification state (i.e. up to 98%TD) was reached after 4 hours of heat treatment at 1600°C and beyond. In addition, ESEM observations showed a major effect of yttrium on grain size due to solute drag effects. Sintering maps were plotted for all the samples and evidenced different stages driven by densification and grain growth. Grain growth was found to be strongly slowed down for x > 0.01, resulting in high values of relative density correlated to submicrometric grain size. Also, activation energies related to densification and grain growth were evaluated around 450 and 500-650 $kJ.mol^{-1}$, respectively. These results led to deliver guidelines for the formulation and sintering of $Th_{1-x}Y_xO_{2-x/2}$ ceramics in prospect of their use as a solid electrolyte.

Keywords : *yttria-doped thoria, densification, grain growth, sintering map, microstructure.*

1. INTRODUCTION

In the framework of the development of the fourth generation of nuclear reactors, which aims to provide safer and resource-saving electronuclear energy, a Sodium-cooled Fast Reactor (SFR) is in a basic design phase in France [1]. In this concept, the peculiar chemistry of liquid sodium contained in the primary vessels must be monitored carefully. Particularly, the oxygen content must be kept under a specific value (usually few ppm), as it controls the corrosion rate of the stainless steel claddings [2]. The use of potentiometric sensors, in which the difference of oxygen activity between environing sodium and an internal reference induces a voltage drop according to Nernst's law, is then currently envisaged. In such systems, the reference and the sodium are separated by a solid electrolyte, which can be brazed on a metallic tube. This electrolyte material should be compatible with sodium at high temperature (about 400°C), mechanically resistant and purely ionic conductor [3]. In this context, the use of yttria-doped thoria electrolyte (*i.e.* $Th_{1-x}Y_xO_{2-x/2}$) was early suggested [4]. Several methods were then used to produce mixed oxides, going from powder metallurgy processes (i.e. mechanical mixtures of pure oxides) [5] to wet chemistry methods which generally yield to homogenous solid solutions [6,7]. The incorporation of Y^{3+} in the fluorite-type structure of ThO_2 (space group Fm-3m) produces oxygen vacancies which turns the ceramic into an ionic conductor [8]. Moreover, doped thoria was generally reported to be much less sensitive to sodium corrosion compared to zirconia, which is frequently used in oxygen sensors [9].

Conversely to elaboration methods and assessment of the electrical properties, the sintering of yttria-doped thoria and the control of its final microstructure was rarely addressed in the literature. Yet, operating in an extreme environment such as liquid sodium generates important requirements on the electrolyte microstructure, including fine grain size and high density, in order to resist to sodium corrosion and mechanical stress [7]. The elaboration of a sintering map, which links the grain size with the relative density [10], then appears as a very important tool to foresee the final microstructure of the electrolyte. However, very few papers in the literature dealt with the elaboration of sintering maps for actinide-based materials, including dioxides. Particularly, the densification of ThO_2 was mainly studied as a function of the preparation route [11,12], specific surface area of the starting powder [13] or content in doping actinide elements, including uranium and plutonium [14,15]. Predictive studies were only reported recently by Kutty *et al.* who established the Master Sintering Curve of ThO_2 doped with 0.5 wt% of CaO [16] or with U_3O_8 [14], as well as by Clavier *et al.* [17] who plotted the sintering map of ThO_2 using HT-ESEM observations coupled to dilatometry measurements. Also, the mechanisms driving the densification of M^{3+}-doped ThO_2 remain

widely unknown [18]. Mainly divalent (CaO) [19] and pentavalent metal (Nb_2O_5, …) [20,21] oxides were studied as sintering aids for thoria, although with few hints concerning the effect of the doping ratio. Moreover, the few studies dedicated to the densification processes in the ThO_2-Y_2O_3 system mainly started from mixtures of powders [22] while the development of wet chemistry routes, which directly yield to homogenous solid solutions as raw powder material, can induce major modifications in the diffusion mechanisms operating during the sintering at high temperature.

In this context, we undertook an exhaustive study dedicated to the sintering of $Th_{1-x}Y_xO_{2-x/2}$ solid solutions initially prepared from oxalic route. First, a classical dilatometric study led to assess the optimal operating conditions in terms of heating temperature and duration to achieve the complete densification of the pellets. The sintering maps of several yttria-doped thoria were then plotted, with the aim to provide guidelines for the elaboration of electrolyte materials to be operated in liquid sodium. Finally, the mechanisms responsible for densification and grain growth were assessed for several yttrium contents and associated activation energies were determined.

2. EXPERIMENTAL

2.1 PREPARATION AND CHARACTERIZATION OF $(Th_{1-x}Y_x)O_{2-x/2}$ OXIDE POWDERS

All the chemicals used during the preparation of the powdered samples, including thorium nitrate $Th(NO_3)_4.5H_2O$, were supplied by Sigma-Aldrich and were of analytical grade (purity ≥ 99%). As already reported in our previous works [23], thorium-yttrium mixed oxides, $Th_{1-x}Y_xO_{2-x/2}$ ($0.01 \leq x \leq 0.22$), were prepared through the initial precipitation of oxalate-type precursors following a protocol similar to that described by Horlait *et al.* [24]. Thorium and yttrium nitrate salts were first dissolved in 1M HNO_3 in order to reach a final concentration in cations close to 0.5M. The two solutions were then mixed together in the desired stoichiometry then poured quickly in a beaker containing a large excess of oxalic acid. The solid phase instantaneously formed was quickly separated by centrifugation at 4500 rpm (typically less than 1 minute after precipitation) to avoid grain growth and preserve powders' reactivity. The precipitate was finally washed several times with deionized water then ethanol, and then dried overnight in an oven at 90°C. By these means, quantitative precipitation (*i.e.* > 99.8%) of both thorium and yttrium was achieved, as previously evidenced by ICP-AES measurements conducted on both supernatants and solid phases [23].

Oxide powders were further obtained by thermal conversion of the oxalate precursors at 600°C during 4 hours (air atmosphere). Such operating conditions both allowed an efficient elimination of the residual carbon coming from the decomposition of the organic parts of the precursors, and a good reactivity of the final powders in terms of specific surface area [23]. This latter parameter was evaluated thanks to a Micromeritics Tristar 3020 apparatus using BET method based on nitrogen adsorption/desorption at 77K. Before the analyses, the samples were outgassed at 90°C for 4 hours to eliminate the water molecules adsorbed onto the surface of the solids.

Additionally, SEM observations were carried out thanks to a FEI Quanta 200 ESEM FEG microscope equipped with a Large Field Detector (LFD) and a Back-Scattered Electron Detector (BSED). A low acceleration voltage of 5-10 kV coupled with low vacuum conditions (50 Pa water vapor) was chosen to observe the samples without any additional preparation step such as metallization.

2.2 THERMAL ANALYSES AND SINTERING

Pellets preparation and sintering. Before sintering, oxide samples were pelletized by uniaxial pressing (200 MPa) at room temperature. Typical mass used was about 200 mg, resulting in green pellets of 8 mm in diameter and about 1.3 mm in height (green density ≈ 45%). For sintering purposes, green pellets were further placed in graphite boats and heated between 1400 and 1700°C for 2 to 8 hours in a graphite furnace (AET Technologies) under primary vacuum. A rate of 10°C.min^{-1} was systematically applied on heating while natural cooling was used down to room temperature.

Density measurements. Density of the sintered samples was first determined by geometrical measurements of the dimensions of the pellets with the help of a precision calliper. The obtained values, so called geometric densities, led to an estimation of the global porosity within the samples. In parallel, relative densities, which accounts for the contribution of closed porosity, were determined by helium pycnometry measurements, thanks to a Micromeritics Accupyc 1340 apparatus. Open porosity was then determined by difference of the results obtained through these two complementary techniques. An uncertainty of about 1% was systematically considered for density values, which came from the precision of the calliper used and on the geometrical defects of the pellets, on the one hand, and from the small amount of sample analyzed by He-pycnometry, on the other.

Dilatometry. Dilatometric measurements were conducted on a Setaram Setsys Evolution apparatus, with two distinct protocols. The first one aimed to evaluate the optimal sintering temperature of the $Th_{1-x}Y_xO_{2-x/2}$ oxides for the various compositions considered. Samples were initially disposed between two alumina platelets, and then heated up to 1600°C under air flow, considering a heating rate of 10°C.min^{-1}. Natural cooling was further operated down to room temperature.

Dilatometric measurements were also undertaken in order to estimate the activation energy associated with the densification of the samples. In this purpose, the Dorn's method [25–27], based on incremental isothermal heat treatments, gave a fast and direct access to E_A values. The shrinkage rate of a sample, *i.e.* $v = d(\Delta l/l_0)/dt$, was first recorded at a temperature T_1, then at a temperature T_2 slightly higher than T_1, so that no significant microstructural changes occurred in the sample. During this study, samples were initially placed between two graphite platelets, then heated up under vacuum between 1500°C and 1650°C, considering a dwell time of 30 min each 25°C.

In these conditions, the following equality is obtained:

$$\left(\frac{\Delta l}{l_0}\right)_{end\ step\ T_1} = \left(\frac{\Delta l}{l_0}\right)_{beginning\ step\ T_2} \quad (1)$$

The ratio between the corresponding shrinkage rates can thus be expressed as [17,28]:

$$\frac{v_2}{v_1} = \frac{T_1}{T_2}\exp\left(\frac{-E_A}{R}\left(\frac{1}{T_2}-\frac{1}{T_1}\right)\right) \quad (2)$$

From which the activation energy can be deduced:

$$E_A = \frac{R\times T_1\times T_2}{T_2-T_1}\ln\left(\frac{T_2\times v_2}{T_1\times v_1}\right) \quad (3)$$

Electronic microscopy and image processing. Prior to SEM observations, sintered pellets were polished to reach an optical grade (1µm diamond spray). Grain boundaries were further revealed by thermal etching (heat treatment of 30 min at 1300°C) which was considered not to modify significantly the microstructure of the samples [29]. Several images (typically 4 to 8) were recorded on each sample in order to reach good representativeness. High vacuum

conditions, associated to a very low accelerating voltage (2 – 3.1 kV), were chosen to obtain high resolution images.

SEM images were then processed using successively ImageJ [30] and Gimp softwares [31] in order to determine average grain size as well as grain size distribution. In this aim, grain boundaries were manually drawn, leading to populations of 250 to 600 grains per image, depending on the image quality and the heat treatment applied to the sample. In these conditions, the average grain size could be obtained with a relative discrepancy of 2% [32]. Finally, the equivalent disc diameter was determined for each operating condition with the ImageJ software, using the tetrakaidecahedral grain model established by Coble [33].

3. RESULTS AND DISCUSSION

3.1 CHARACTERIZATION OF THE POWDER SAMPLES

Oxide powders prepared from the thermal conversion of oxalate precursors were first analyzed by SEM (**Figure 1**), in order to evaluate the impact of the yttrium incorporation ratio over morphology. Whatever the chemical composition considered (i.e. x = 0.01; 0.08; 0.15 and 0.22), the powder appeared to be composed by small square-shape platelets of about 1µm in edge, that further assembles to form bigger aggregates. Such a morphology was frequently described in the literature for Th-based oxalates [11,34], and was generally reported to be retained upon calcination during conversion into oxide form [24,35]. Nevertheless, the short aging time considered during the precipitation process in this study led to significantly decrease the size and the thickness of the square-shape platelets (about a factor of 2) in comparison of what was observed in our previous work [23]. Also, one can note that the samples obtained for x = 0.22 exhibited additional smaller needle-like objects that came from the initial precipitation of a polyphase oxalate compound [23,36].

Associated specific surface areas of both oxalate precursors and oxide powders were evaluated by the means of BET measurements and are gathered in **Table 1**, while reference values for pure ThO_2 prepared from similar protocol are supplied for comparison purposes. The specific surface area values for oxalate powders typically varied between 5 and 10 $m^2.g^{-1}$ whereas that of oxides ranged from 6 and 30 $m^2.g^{-1}$. Such trend, which corresponds to an increase in the surface area during the thermal conversion, was already explained by several authors by the decomposition of oxalate entities into CO and CO_2 gaseous molecules and the subsequent formation of mesopores within the powder [35,37]. However, one can note that

the gap between oxalate and oxide powders significantly depends on the chemical composition, leading the specific surface area of oxide powers to decrease with the yttrium content. Indeed, increase in the specific surface area upon heating seems to be favored by low yttrium content (typically for x = 0.01 and x = 0.08), while surface remained almost unchanged for higher incorporation ratios. This observation might be linked with the formation of slightly heterogeneous oxalate compounds for the highest x values investigated. This cation heterogeneity might weaken specific zones of the grains, such as the crystallite boundaries, thus facilitating the elimination of gaseous species during the thermal conversion of oxalate. Such an effect should be even more significant for x = 0.22 which initially led to a polyphase oxalate sample with different decomposition kinetics.

Finally, the density of the oxides studied herein was also calculated, using unit cell parameters reported in the literature for the oxides [23]. Such values will further be used for the determination of the relative densities during the investigations undertaken on sintered pellets.

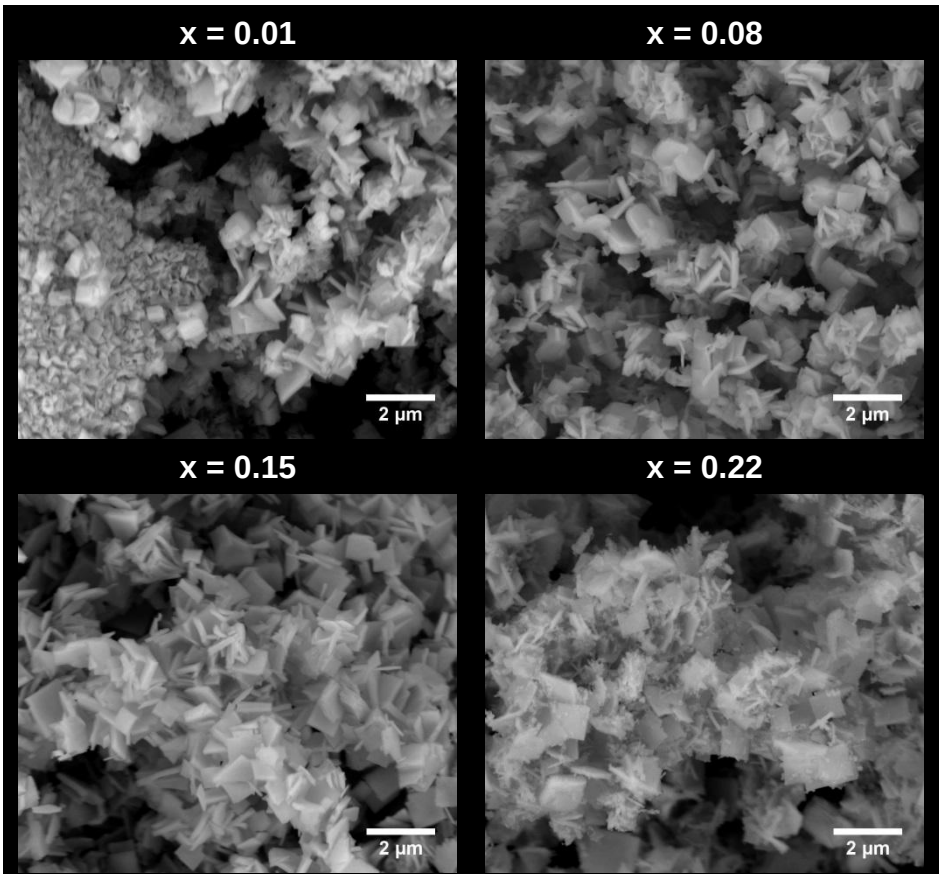

Figure 1 : *SEM observations of the $Th_{1-x}Y_xO_{2-x/2}$ samples obtained after thermal conversion of oxalate precursors (T = 600°C, t = 4 hours, air).*

Table 1 : *Physico-chemical features of oxalate and oxide samples.*

Composition	***Specific surface area ($m^2.g^{-1}$)***		***Calculated density ($g.cm^{-3}$)***
	Oxalate	***oxide***	
x = 0	/	9 to 13 [38]	9.97 [39]
x = 0.01	10	30	9.95 [23]
x = 0.08	7	11	9.58 [23]
x = 0.15	5	6	9.24 [23]
x = 0.22	7	7	8.88 [23]

Uncertainly attached to the determination of specific surface area : ± 1 $m^2.g^{-1}$

3.2 DETERMINATION OF OPTIMAL SINTERING CONDITIONS

3.2.1 Dilatometric study

The determination of the operating conditions required to reach full densification of oxide samples was undertaken through dilatometric measurements. The variation of the relative linear shrinkage of the pellets versus temperature, presented in **Figure 2**, appears to be very similar whatever the yttrium content even if the shrinkage could appear slightly faster for x = 0.01, which was ascribed to the high value reached by the specific surface area for this sample (**Table 1**) and/or to a more rapid homogenization of the Th/Y distribution in the solid prior to the densification processes in this case [23].

For all of our samples, the shrinkage can be described in two steps. The first one, which took place between 800°C to 1200°C, can be assigned to the crystallite growth within the square-shape platelets constituting the powder. Conversely, the second one, starting around 1400°C, is more likely to correspond to the sintering between these platelets and led to a more pronounced shrinkage rate, hence to a more efficient densification process. Such a two-step process was frequently described during the sintering of actinide oxides initially prepared *via* oxalic precipitation [34,40]. It likely arises from the formation of micrometric particles composed of nanoscale crystallites after the thermal conversion of oxalate precursors, which further led to crystallite growth and densification phenomena within the square-shape platelet, as attested by several authors based on XRD measurements and *in situ* ESEM observations [41].

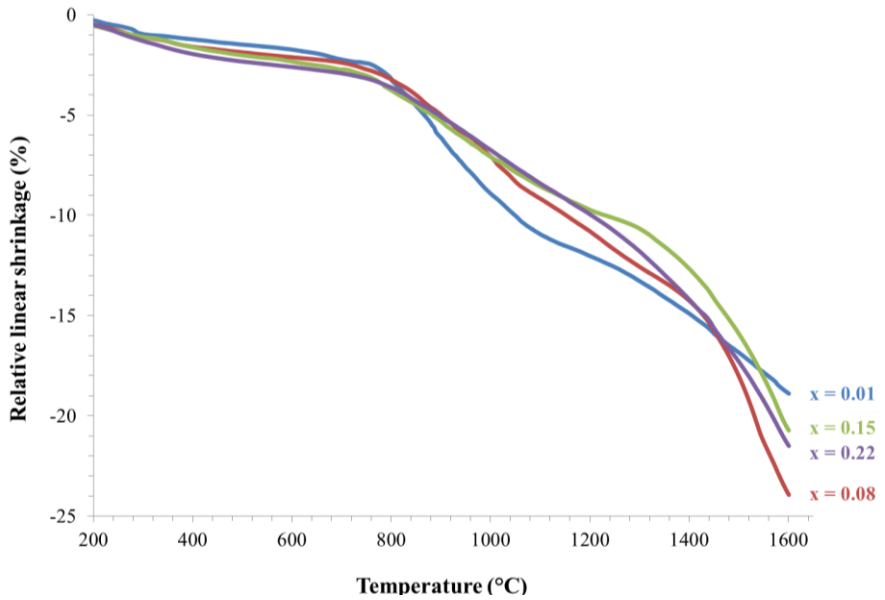

***Figure 2** : Variation of the relative linear shrinkage of $Th_{1-x}Y_xO_{2-x/2}$ solid solutions pellets versus temperature.*

Also, one can note that no plateau was clearly evidenced at the end of the experiments, meaning that the densification was still incomplete after 10 minutes of heating at 1600°C. This result was confirmed by the geometrical density values collected after dilatometric measurements, which systematically lied around 90% whatever the yttrium content. Moreover, these observations appear to be consistent with the data reported in the literature for pure ThO_2, since a full densification was generally obtained between 1500 and 1700°C depending on the nature of the starting powder and the sintering conditions [13,42]. On this basis, the final densification was undertaken at or above 1600°C, considering an isotherm dwell of one to several hours.

3.2.2 Variation of the density versus operating conditions

In order to confirm the results obtained from dilatometric measurements, the density of $Th_{1-x}Y_xO_{2-x/2}$ sintered samples was evaluated for four sintering temperatures (1400, 1500, 1600 and 1700°C) and four heating times (1, 2, 4 and 8 hours). The values of geometrical density generally increased up to 96-98% for a heat treatment of 4 hours at 1600°C, in good agreement with the dilatometry study (**Figure 3**). Lower heating temperatures, i.e. typically 1400 and 1500°C only allowed to trigger first [43] then intermediary step of sintering [44], which respectively correspond to the formation of necks between grains then to the elimination of open porosity. Also, one can note that lower density values were systematically measured for x = 0.01, in spite of the highest sintering rate observed from dilatometry, which might indicate a different sintering mechanism for this composition.

For higher heating temperatures or longer heating times, the density was found to remain constant in the upper range of values measured (i.e. typically above 95% of the calculated value), meaning that the sintering process was mostly driven by grain growth processes in these operating conditions [44]. Also, such domain of densities confirms that the final stage of sintering, generally characterized by the elimination of closed porosity [44], was reached (see He pycnometry data supplied as supplementary material in **Table S1** for x = 0.01 and **Table S2** for x = 0.08).

The complete densification of the samples was also confirmed by SEM observations performed on samples sintered during 8 hours at 1600°C (**Figure 4**). Whatever the yttrium content considered, no open porosity was detected while the grain size appeared to be homogenous. Nevertheless, the grain size was found to be strongly dependent on the chemical composition. Indeed, it ranged from 0.5 to 4.2 µm for $Th_{0.99}Y_{0.01}O_{1.995}$ (average value of 1 ± 0.5 µm) while for higher yttrium contents (x = 0.08, 0.15 and 0.22), the distribution of the grain sizes remained between 0.1 and 0.9 µm (average : 0.4 ± 0.2 µm) (see grain size distributions data of x = 0.01 and x = 0.15 supplied as supplementary material in **Figure S1**).

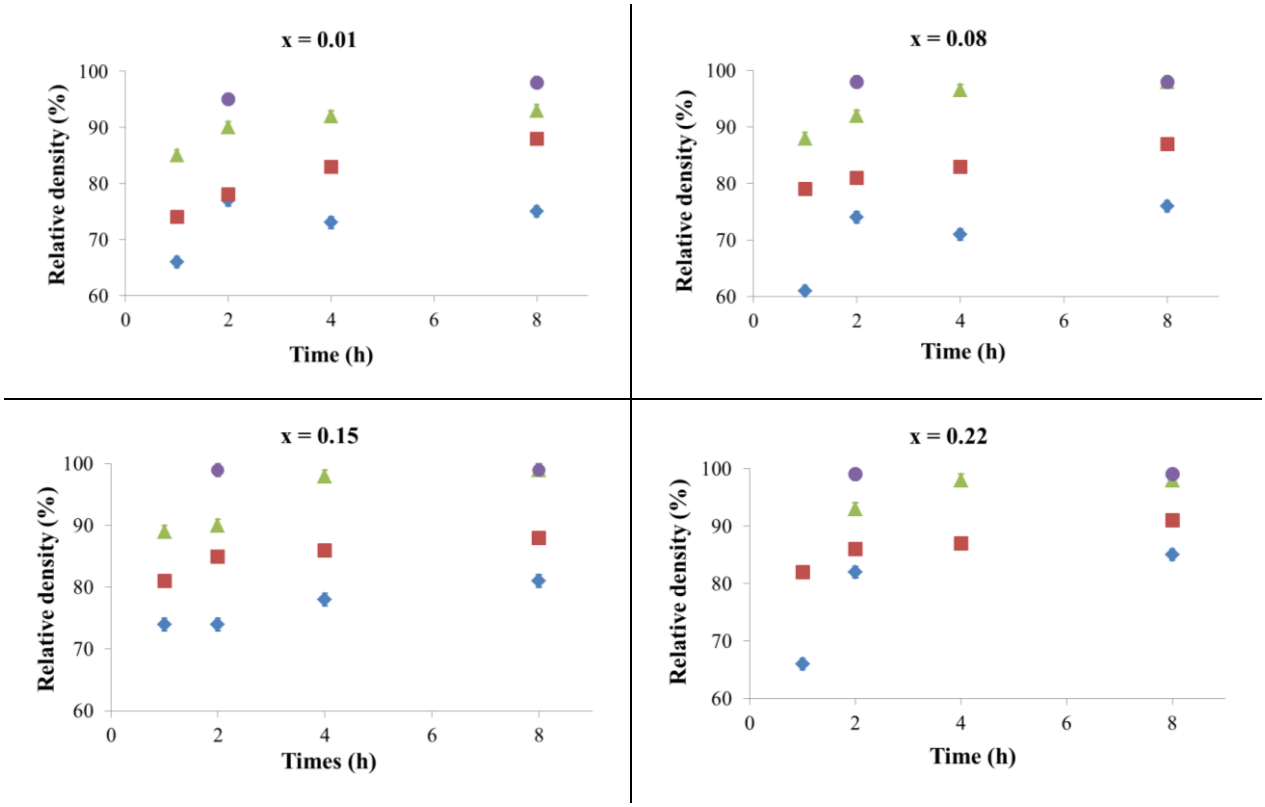

***Figure 3** : Variation of the relative density versus heating time at different temperatures (1400°C - ◆, 1500°C - ■, 1600°C - ▲, 1700°C - ●) for several $Th_{1-x}Y_xO_{2-x/2}$ samples.*

Cosentino *et al.* already noticed similar discrepancies [6], the density of their samples increasing with yttrium content in the $0.06 \leq x \leq 0.18$ range. Comparable observation was made for 5 and 10 mol.% yttria-doped ThO_2 by Purohit *et al*. They explained the difference of densification state from the higher number of defects (oxygen vacancies) present in $Th_{0.9}Y_{0.1}O_{1.95}$ [45]. Nevertheless, whereas these authors argue for a continuous effect of the doping ratio, the strong difference noticed in our study between x = 0.01, on the one hand, and for $0.08 \leq x \leq 0.22$, on the other hand, suggests that a threshold value of the yttrium doping ratio (typically a few percent in mole) could hinder grain growth. Such behavior was reported in Y-doped zirconia but was generally correlated to the structural modifications caused by doping (the tetragonal lattice stabilized for 2 mol.% Y being more favorable to grain growth than the cubic one obtained for 8 mol.% Y) [46],[47]. However, such crystallographic effect did not occur for $Th_{1-x}Y_xO_{2-x/2}$ since previous work demonstrated that the fluorite-type structure is stable on the whole range of composition studied [23].

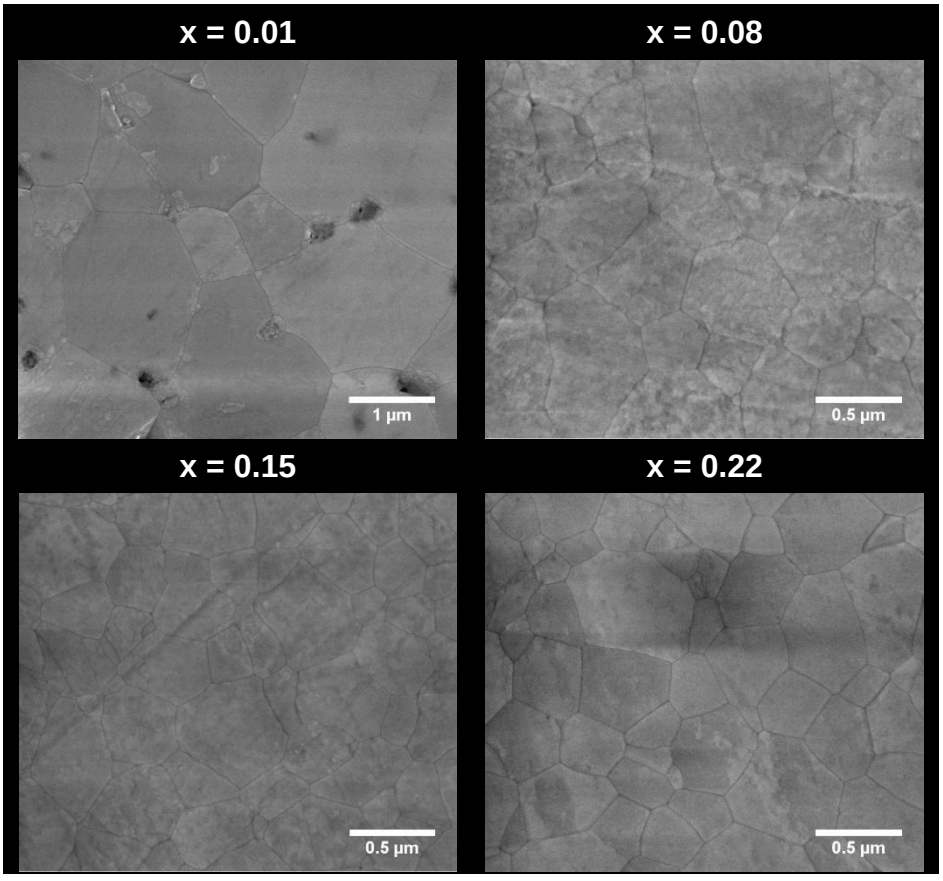

***Figure 4** : SEM observations of $Th_{1-x}Y_xO_{2-x/2}$ pellets after sintering at 1600°C during 8 hours.*

More likely, the inhibition of grain growth above x = 0.01 could be linked to the establishment of solute drag effect. Indeed, when doping a fluorite-type oxide with acceptor

dopant, charge-compensating defects are formed in the oxygen sub-lattice, which strongly enhances oxygen diffusion. Cations then become the rate-limiting species in the system. However, dopants were frequently reported to segregate to the grain boundary, resulting in a solute drag, so that grain boundary mobility is controlled by the lattice diffusion of the dopant [48,49]. On this basis, small amounts (i.e. typically below 1%) of dopants, such as CaO, TiO_2 or Cr_2O_3, were already proved to significantly enhance the sintering of MO_2 compounds (with M = Ce, Th, U, Pu) [50-[52]. The formation of anion vacancies also increases the migration of cations, then promoting grain boundary mobility and grain growth [53]. On the other hand, higher values of doping generally led to grain growth inhibition [51,54]. Particularly, yttrium was found to strongly limit the grain growth processes in CeO_2 [49] and ZrO_2 [55] samples over 1% of doping. Correlatively, the slightly heterogeneous distribution of the cations in the starting powders evidenced in our previous work [23] could also induce grain growth inhibition for the highest yttrium contents considered. Indeed, the progressive homogenization of the yttrium distribution in the structure under cation interdiffusion was found to occur beyond 1400°C and could delay, if not hinder, the grain growth process. One can suppose that such heterogeneity effects become more and more significant with increasing yttrium content. Finally, complex defects such as vacancies clusters could also form [51], then limiting the diffusion within the sample.

3.3 SINTERING MAP

The sintering map of a ceramic material represents the variation of the average grain size as a function of the relative density under different densification conditions, including temperature, heating time or chemical composition. It thus constitutes a performant tool to design targeted microstructures, in order to reach the requirements linked to the various domains of application of ceramic materials. As a matter of fact, several examples were reported in the literature, either for the complex magnetic permeability of ferrite system [56], ultrapure alumina [57], or more recently on niobium-doped titania [58] or YAG ceramics [59,60]. However, only one set of data was reported by Clavier *et al.* [17] on radioactive material (*i.e.* ThO_2) by combining *in situ* HT-ESEM observations and dilatometry. Such lack of data probably arose from the important number of experiments needed coupled to the hazards associated to handling of radioactive materials.

The samples prepared in this work (sintering temperature : 1400-1700°C; dwell time : 1-8 hours) were used to establish sintering maps for the different $Th_{1-x}Y_xO_{2-x/2}$ solid solutions

studied. In this aim, geometrical measurements were used to reach relative densities, while SEM micrographs performed on polished surfaces and further image analysis led to average grain size. The resulting sintering trajectories for x = 0.01; 0.08, 0.15 and 0.22 are plotted in **Figure 5**. Whatever the composition considered, two different processes can be identified during sintering, in good agreement with the trends generally observed in the literature for sintering maps [17,56–61]. The first one corresponds to a densification-driven step with a rapid increase of the density but limited grain growth. Conversely, the second step was characterized by prevailing grain growth with limited additional densification up to 98-99%. Moreover, Bernache-Assolant *et al.* reported that the limit between the two processes is generally found around 92% [62] which is also the case in our study.

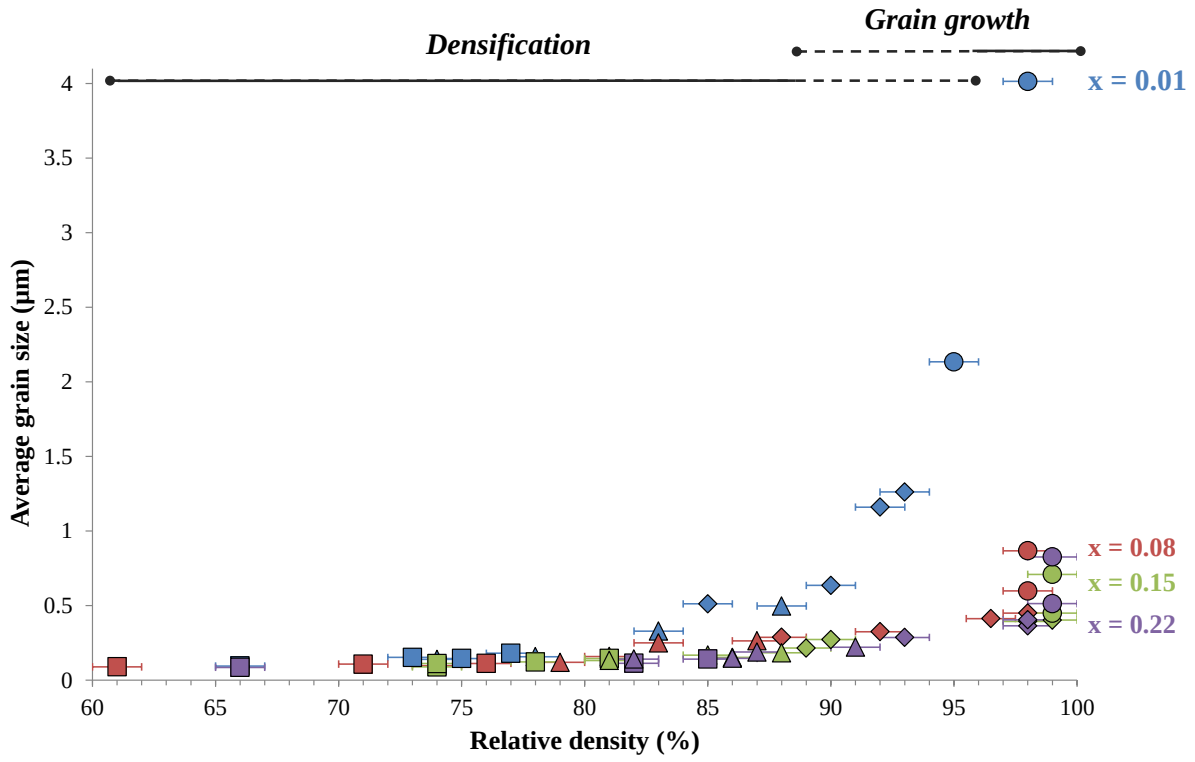

***Figure 5** : Sintering trajectories of $Th_{1-x}Y_xO_{2-x/2}$ ceramics (1400°C - □, 1500°C - △, 1600°C-◇, 1700°C-○) (x = 0.01 – **Blue**, x = 0.08 – **Red**, x = 0.15 – **Green**, x =0.22 – **Purple**).*

Beyond this general trend, the sintering maps also again evidence different microstructural evolutions depending on the yttrium content. Indeed, high doping ratios (x > 0.01) led to a pure densification step (i.e. without simultaneous and significant grain growth) up to 95-96% of the calculated density. As previously stated, in this case, the grain growth is probably slowed down by solute drag effects. Moreover, the small granulometry of the

starting powder probably strengthen this effect, due to the high grain boundary area per unit volume [63]. Nevertheless, the use of relatively high temperature of heating (typically 1600 or 1700°C) can still allow a limited grain growth. Conversely, the grain growth stage starts as soon as from 83% of relative density for x = 0.01 and operates concomitantly with densification, probably due to the lower solute drag effect occurring for this sample. On this basis, it was not possible to prepare highly densified ceramics with submicrometric grain size for this particular composition. Since the use of a ceramic electrolyte in liquid sodium media requires very dense and fine grains materials to resist corrosion [7], the use of yttrium doping ratio around 1 mol.% should then be avoided. Conversely, high yttrium contents must be favored, the final choice being completed on the basis of the electrical properties and the resistance to corrosion damage.

3.4 SINTERING MECHANISMS

The microstructural evolution of porous ceramic materials can be monitored through grain growth, which is frequently described by the following equation [64] :

$$D^n - D_0^n = kt \qquad (4)$$

With k depending on the temperature following an Arrhenius law such as

$$k = k_0\, e^{\left(\frac{-Ea}{RT}\right)} \qquad (5)$$

where D is the average grain size at time t, D_0 is the initial grain size, k_0 is a rate constant and n is a whole number depending on the diffusion mechanism responsible for grain growth. Typically, for solid solutions in which dopant might segregate to grain boundaries, n = 2 accounts for a solute drag effect with high solubility of the dopant (i.e. to a behavior close to a pure ceramic), while n = 3 corresponds to a low solubility [44].

When D_0 is much smaller than D, i.e. in the case of nanoscale starting powders, the grain growth expression can be simplified by neglecting D_0^n in comparison with D^n. Then, the equation can be simplified as follows [50]:

$$D^n = k_0\, e^{\left(\frac{-Ea}{RT}\right)} t \qquad (6)$$

This equation was established considering that the granulometric distribution within the sample remains similar whatever the heating duration. In this hypothesis, the normalized distribution should be invariant as a function of time [65]. Several authors were able to show experimentally the self-similarity of grain size distribution as a function of time for ceramic systems [28,32]. Monte Carlo calculations were also used to model grain growth and showed that the grain size distribution function was independent of time for each grain class [66]. This self-similarity is a result of invariance of each grain class (with a constant ratio x = D/Dmean) as a function of time.

In the present work, a systematic study of the grain growth of $Th_{1-x}Y_xO_{2-x/2}$ ceramics was undertaken by varying sintering temperature and duration for several yttrium contents. As a matter of example, **Figure 6** shows the conservation of the grain size distribution for $Th_{0.92}Y_{0.8}O_{1.96}$ at 1600°C. Whatever the heating time chosen between 1 and 8 hours, the distribution of the relative grain size systematically follows the same sigmoidal trend, thus demonstrating that it could be considered as a normal distribution. Hence, no exaggerated grain growth phenomena took place during the various heat treatments performed. Also, similar results were obtained whatever the chemical composition and the sintering temperature considered, showing that a modification of the yttrium content did not induce any heterogeneous grain growth processes.

Based on a normal grain growth distribution, it was then possible to assess the mechanism driving the grain growth through the determination of the n exponent value. This latter can be determined from the slope of the plot of $ln(D)$ versus $ln(t)$ as shown in equation (7) :

$$n\ln(D) = \ln(t) - \frac{Ea}{RT} + \ln(k_0) \qquad (7)$$

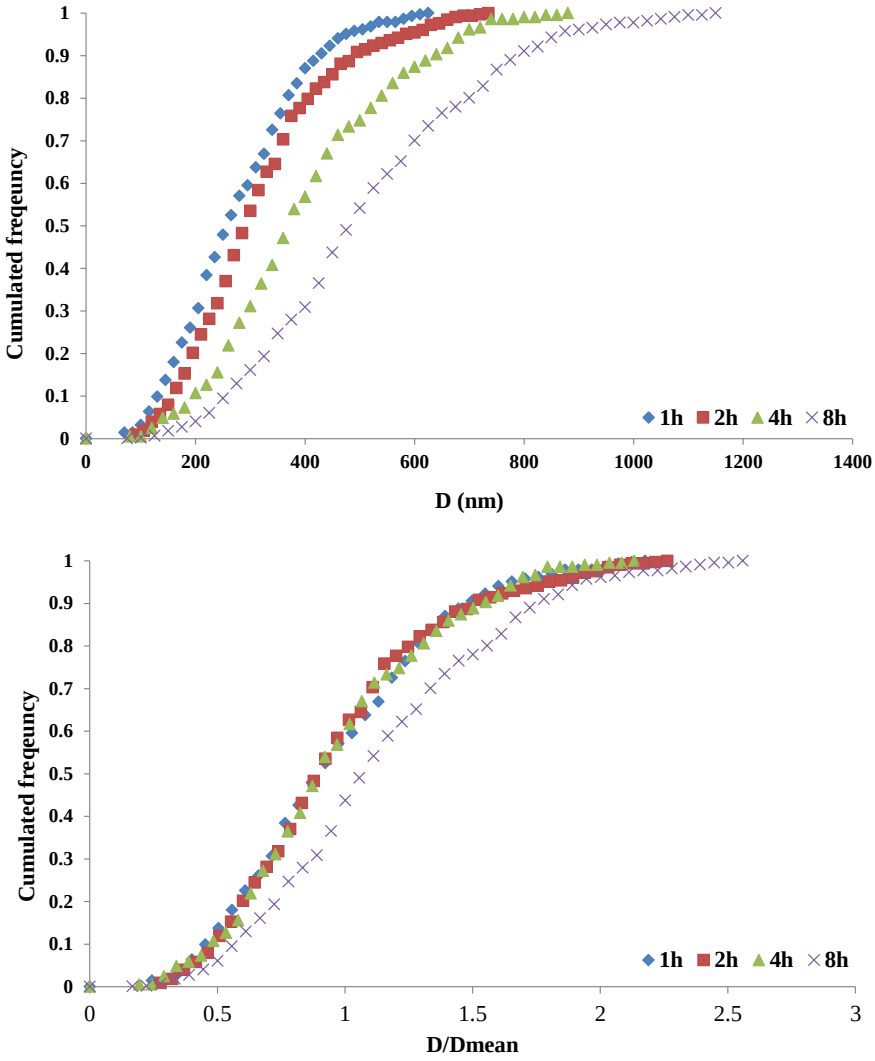

Figure 6 *: Conservation of grain size distribution at 1600°C for* $Th_{0.92}Y_{0.08}O_{1.96}$.

Whatever the yttrium doping ratio and the operating conditions investigated, the plot of ln(*D*) versus ln(*t*) was found to be linear (**Figure 7**). However, different behaviors were observed, meaning that different mechanisms were involved depending on the operating conditions considered. First, all the experiments undertaken at 1400°C led to a value of the n exponent close to 4. As this heating temperature was correlated to relative densities below 85% of the calculated value, one could then suggest that initial and intermediate steps of $Th_{1-x}Y_xO_{2-x/2}$ sintering are controlled by pore mobility, and driven through grain boundary diffusion. This result is in good agreement with previous studies performed on doped-ThO_2 ceramics [19,50], and with the latest observations collected *in situ* by Nkou Bouala *et al.* on ThO_2 microspheres [67], which already evidenced the predominance of grain boundary diffusion during the densification step.

For higher temperatures, the results obtained varied with the yttrium content and confirmed the peculiar behavior of the $Th_{0.99}Y_{0.01}O_{1.995}$ compounds, already suggested by SEM observations and sintering maps. Indeed, all the samples prepared with x = 0.01 led to $n = 2$, *i.e.* to a strong solubility of the yttrium dopant in the ThO_2 lattice, either in the bulk material or at the grain boundary. Such a result then backs up the hypothesis of a low solute drag effect, which subsequently does not hinder significantly the grain boundary mobility. Conversely, higher yttrium amounts, *i.e.* from 8 to 22 mol.%, led to *n* values above 2 (mostly close to 3). In this case, the segregation of yttrium to the grain boundary is then probably more important, resulting in an important solute drag effect, in good agreement with the smaller grain size observed by SEM.

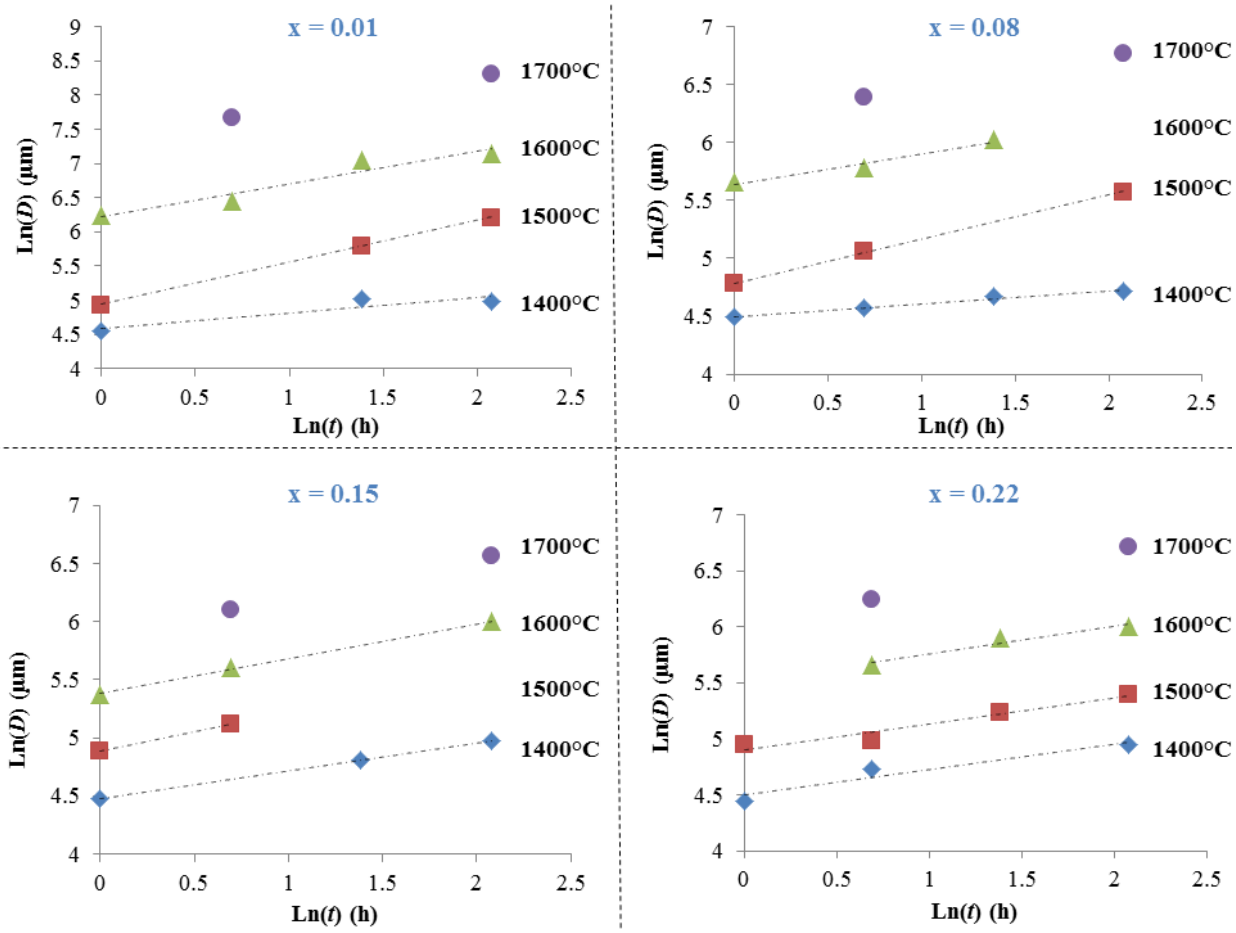

***Figure 7** : Variation of ln(D) versus ln(t) to determine the n value of $Th_{1-x}Y_xO_{2-x/2}$ oxide (1400°C - ◆, 1500°C - ■, 1600°C - ▲, 1700°C - ●).*

According to equation (6) and the values determined for *n* in the 1500-1700°C range (*i.e.* $n = 2$ for x = 0.01 and $n = 3$ for x > 0.01), it was also possible to evaluate the activation

energy linked to grain growth during the sintering of the four samples considered. The results obtained (**Table 2**) demonstrate once again a specific behavior for low amount of dopant. Indeed, for x = 0.01, the E_A value reached up to around 670 kJ.mol^{-1} while it was found close to 500 kJ.mol^{-1} for the other compositions investigated. Such an important gap is consistent with the modification of the mechanism responsible for grain growth when modifying the doping ratio. Also, the high value of activation energy determined for x = 0.01 fits well with the increased grain growth observed at high temperature for this sample. Besides, one can note that all the values obtained in this work remain in the same range of magnitude than those previously reported in the literature for ThO_2 ceramics, in presence or not of sintering aids, which are generally found between 500 and 650 kJ.mol^{-1} [42,68,69].

Table 2 : Determination of activation energy for each yttrium content from Dorn's method and the grain growth method in comparison with the literature

Oxide	***Ea (kJ.mol^{-1})***		***Reference***
ThO_2	650		[68,69]
ThO_2 – 0.5 wt% CaO	525		[42]
ThO_2	435 ± 25		[17]
	Densification (Dorn's method)	**Grain growth**	
$Th_{0.99}Y_{0.01}O_{1.995}$	425 ± 30	672 ± 33	
$Th_{0.92}Y_{0.08}O_{1.96}$	450 ± 30	536 ± 27	This work
$Th_{0.85}Y_{0.15}O_{1.925}$	/	507 ± 30	
$Th_{0.78}Y_{0.22}O_{1.89}$	/	557 ± 56	

Additional tests were finally undertaken thanks to the Dorn's method, which was usually used in the literature to determine the activation energy (E_A) of sintering from dilatometric measurements, especially in the first stage of the densification process [27]. Dilatometric measurements were then undertaken between 1500 and 1650°C, and applying isothermal dwells of 30 min. with steps of 25°C (**Figure 8**).

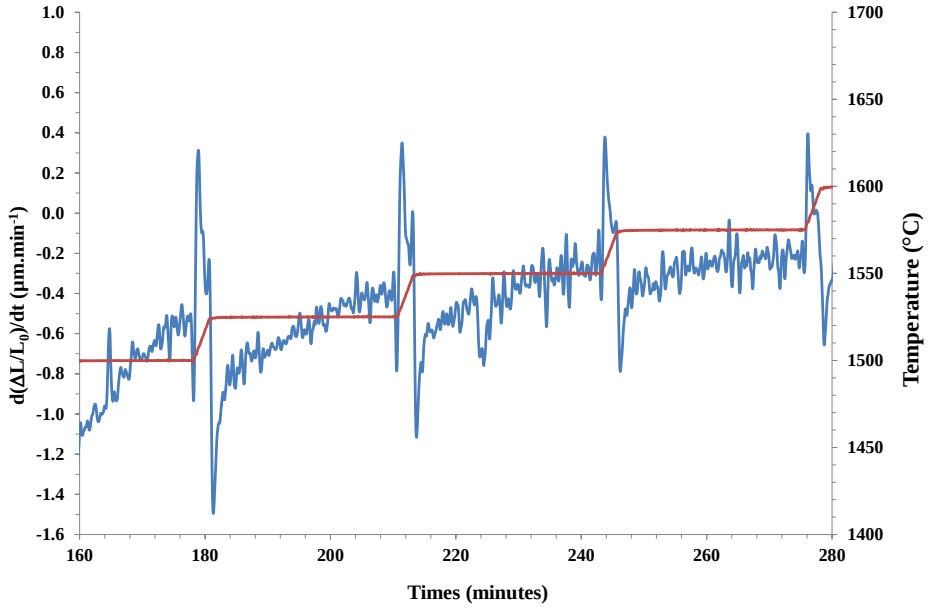

***Figure 8** : Determination of $Th_{1-x}Y_xO_{2-x/2}$ sintering activation energy using the Dorn's method.*

The results obtained for x = 0.01 and x = 0.08 were both found in the 400-450 kJ.mol^{-1} range (**Table 2**). They remain notably lower than those evaluated from grain growth. Nevertheless, owing to the short duration of isothermal dwell, one can suggest that a complete densification of the ceramics was not reached, and that samples were still undergoing first stage of densification. Based on this hypothesis, E_A values obtained from Dorn's method would more likely characterize the initial step of sintering, *i.e.* establishment of necks between the grains. Indeed, they appear in very good agreement with the value recently determined by Nkou Bouala *et al.* for the elaboration of a neck between ThO_2 microspheres [67]. Also, the difference observed between the activation energies measured for densification and grain growth processes are similar with that reported for other materials, such as $LaPO_4$ ceramics [70].

More importantly, it is noteworthy that comparable values were obtained for the two samples studied, meaning that the yttrium doping ratio strongly influences the grain growth but does not present any significant impact over densification. However, as the grain growth rate is limited by solute drag effects for x > 0.01, the reduction of the total surface energy probably proceeds more easily through densification in these samples, resulting in highly dense and fine-grain materials.

4. CONCLUSION

The sintering process of $Th_{1-x}Y_xO_{2-x/2}$ ceramics (x = 0.01, 0.08, 0.15 and 0.22) , including densification and grain growth, was investigated under various operating conditions in terms of temperature and heating time. A densification state fulfilling the requirements linked with the operation of the material in liquid sodium was generally reached beyond 4 hours of heating at 1600°C. Particularly, high densities around 98% were determined after heating for 8 hours at 1700°C, whatever the yttrium content was. Moreover, the variation of the relative density was plotted as a function of the average grain size to construct sintering maps. These data clearly evidenced a different behavior of the x = 0.01 sample compared to compounds doped with higher yttrium amounts. Particularly, an increased grain growth was observed, which precludes the preparation of ceramics presenting both high densification state and submicrometric average grain size. Such difference was assigned to strong solute drag effects for high yttrium contents (typically above 1%) which inhibit grain growth during the sintering process. This difference was also enlightened by the determination of the corresponding activation energies, which differ significantly with the yttrium content for grain growth (typically from 500 to about 670 $kJ.mol^{-1}$) while it remains close to 450 $kJ.mol^{-1}$ for the densification process. This study then shed light on the fundamentals of the microstructural development of $Th_{1-x}Y_xO_{2-x/2}$ ceramics. It also led to deliver guidelines for the fabrication of electrolyte materials with tailored density and grain size for several doping ratios.

Acknowledgements : The authors are pleased to thank Johann Ravaux for his help in SEM examinations. They are also grateful to CEA for its continuous financial support.

REFERENCES

[1] J.E. Kelly, Generation IV International Forum: A decade of progress through international cooperation, Prog. Nucl. Energ. 77 (2014) 240–246.

[2] L. Brissonneau, New considerations on the kinetics of mass transfer in sodium fast reactors: An attempt to consider irradiation effects and low temperature corrosion, J. Nucl. Mater. 423 (2012) 67–78.

[3] E. Schouler, A. Hammou, M. Kleitz, Complex impedance of electrochemical cells based on yttria doped thoria, Mater. Res. Bull. 11 (1976) 1137–1146.

[4] D.J. Hayes, Instrumentation for liquid sodium in nuclear reactors, J. Phys. E 7 (1974) 69–75.

[5] W.A. Ross, E.T. Weber, Fabrication and Characterization of ThO_2-Y_2O_3 Solid Electrolyte Tubes, Am. Ceram. Soc. Bull. 50 (1971) 787.

[6] I.C. Cosentino, R. Muccillo, Powder synthesis and sintering of high density thoria–yttria ceramics, J. Nucl. Mater. 304 (2002) 129–133.

[7] R. Ganesan, S. Vivekanandhan, T. Gnanasekaran, G. Periaswami, R.S. Srinivasa, Novel approach for the bulk synthesis of nanocrystalline yttria doped thoria powders via polymeric precursor routes, J. Nucl. Mater. 325 (2004) 134–140.

[8] I.C. Cosentino, R. Muccillo, Lattice parameters of thoria–yttria solid solutions, Mater. Lett. 48 (2001) 253–257.

[9] R.G. Taylor, R. Thompson, Testing and performance of electrolytic oxygen meters for use in liquid sodium, J. Nucl. Mater. 115 (1983) 25–38.

[10] S.-J.L. Kang, Y.-I. Jung, Sintering kinetics at final stage sintering: model calculation and map construction, Acta Mater. 52 (2004) 4573–4578.

[11] G.D. White, L.A. Bray, P.E. Hart, Optimization of thorium oxalate precipitation conditions relative to derived oxide sinterability, J. Nucl. Mater. 96 (1981) 305–313.

[12] E. Oktay, A. Yayli, Physical properties of thorium oxalate powders and their influence on the thermal decomposition, J. Nucl. Mater. 288 (2001) 76–82.

[13] K. Ananthasivan, S. Anthonysamy, A. Singh, P.R. Vasudeva Rao, De-agglomeration of thorium oxalate – a method for the synthesis of sinteractive thoria, J. Nucl. Mater. 306 (2002) 1–9.

[14] T.R.G. Kutty, K.B. Khan, P.V. Hegde, A.K. Sengupta, S. Majumdar, H.S. Kamath, Determination of activation energy of sintering of ThO_2-U_3O_8 pellets using the master sintering curve approach, Sci. Sinter. 35 (2003) 125–132.

[15] T.R.G. Kutty, P.V. Hegde, K.B. Khan, T. Jarvis, A.K. Sengupta, S. Majumdar, H.S. Kamath, Characterization and densification studies on ThO_2–UO_2 pellets derived from ThO_2 and U_3O_8 powders, J. Nucl. Mater. 335 (2004) 462–470.

[16] A. Ray, J. Banerjee, T.R.G. Kutty, A. Kumar, S. Banerjee, Construction of master sintering curve of ThO_2 pellets using optimization technique, Sci. Sinter. 44 (2012) 147–160.

[17] N. Clavier, R. Podor, L. Deliere, J. Ravaux, N. Dacheux, Combining in situ HT-ESEM observations and dilatometry: An original and fast way to the sintering map of ThO_2, Mater. Chem. Phys. 137 (2013) 742–749.

[18] A. Baena, T. Cardinaels, J. Vleugels, K. Binnemans, M. Verwerft, Activated sintering of ThO_2 with Al_2O_3 under reducing and oxidizing conditions, J. Nucl. Mater. 470 (2016) 34–43.

[19] S.N. Laha, A.R. Das, Isothermal grain growth and sintering in pure ThO_2 and ThO_2-CaO compositions, J. Nucl. Mater. 39 (1971) 285–291.

[20] T.R.G. Kutty, K.B. Khan, A. Kumar, H.S. Kamath, Densification strain rate in sintering of ThO_2 and ThO_2-0.25% Nb_2O_5 pellets, Sci. Sinter. 41 (2009) 103–115.

[21] A. Yayli, S. Kirtay, E. Oktay, A. Van, M.T. Aybers, L. Çolak, Sintering properties of V_2O_5, Ta_2O_5 and Nb_2O_5 doped ThO_2 powder under Ar-10% H_2 atmosphere, Key Eng. Mater. 264 (2004) 305–308.
[22] G.P. Halbfinger, M. Kolodney, Activated Sintering of ThO_2 and ThO_2-Y_2O_3 with NiO, J. Am. Ceram. Soc. 55 (1972) 519–524.
[23] M. Gabard, Y. Cherkaski, N. Clavier, L. Brissonneau, M.C. Steil, J. Fouletier, A. Mesbah, N. Dacheux, Preparation, characterization and sintering of yttrium-doped ThO_2 for oxygen sensors applications, J. Alloys Compd. 689 (2016) 374–382.
[24] D. Horlait, N. Clavier, N. Dacheux, R. Cavalier, R. Podor, Synthesis and characterization of $Th_{1-x}Ln_xO_{2-x/2}$ mixed-oxides, Mater. Res. Bull. 47 (2012) 4017–4025.
[25] P. Dehaudt, L. Bourgeois, H. Chevrel, Activation energy of UO_2 and UO_{2+x} sintering, J. Nucl. Mater. 299 (2001) 250–259.
[26] D. Lahiri, S.V. Ramana Rao, G.V.S. Hemantha Rao, R.K. Srivastava, Study on sintering kinetics and activation energy of UO_2 pellets using three different methods, J. Nucl. Mater. 357 (2006) 88–96.
[27] J.J. Bacmann, G. Cizeron, Contribution a l'etude des mecanismes du debut de frittage du bioxyde d'uranium, J. Nucl. Mater. 33 (1969) 271–285.
[28] R. Podor, N. Clavier, J. Ravaux, L. Claparede, N. Dacheux, In Situ HT-ESEM Observation of CeO_2 Grain Growth During Sintering, J. Am. Ceram. Soc. 95 (2012) 3683–3690.
[29] A. Maître, D. Beyssen, R. Podor, Effect of ZrO_2 additions on sintering of SnO_2-based ceramics, J. Eur. Ceram. Soc. 24 (2004) 3111–3118.
[30] ImageJ: Wayne Rasband, http://rsbweb.nih.gov/ij/ (accessed 30.03.2017).
[31] S. Kimball, P. Mattis, Gimp software, GNU Image Manip. Program. (n.d.).
[32] A. Maître, D. Beyssen, R. Podor, Modelling of the grain growth and the densification of SnO_2-based ceramics, Ceram. Int. 34 (2008) 27–35.
[33] R.L. Coble, Sintering Crystalline Solids. I. Intermediate and Final State Diffusion Models, J. Appl. Phys. 32 (1961) 787–792.
[34] N. Hingant, N. Clavier, N. Dacheux, N. Barre, S. Hubert, S. Obbade, F. Taborda, F. Abraham, Preparation, sintering and leaching of optimized uranium thorium dioxides, J. Nucl. Mater. 385 (2009) 400–406.
[35] L. Claparede, N. Clavier, N. Dacheux, A. Mesbah, J. Martinez, S. Szenknect, P. Moisy, Multiparametric dissolution of thorium-cerium dioxide solid solutions, Inorg. Chem. 50 (2011) 11702–11714.
[36] B. Arab-Chapelet, S. Grandjean, G. Nowogrocki, F. Abraham, Synthesis and characterization of mixed An(IV)/An(III) oxalates (An(IV) = Th, Np, U or Pu and An(III) = Pu or Am), J. Nucl. Mater. 373 (2008) 259–268.
[37] D. Dollimore, The thermal decomposition of oxalates. A review, Thermochim. Acta. 117 (1987) 331–363.
[38] N. Hingant, Synthèse, frittage et caractérisation de solutions solides d'oxydes mixtes de thorium et d'uranium (IV) : Influence de la méthode de préparation du précurseur, PhD Thesis, Université de Paris Sud, 2008.
[39] K. Clausen, W. Hayes, J.E. Macdonald, P. Schnabel, M.T. Hutchings, J.K. Kjems, Neutron scattering investigation of disorder in UO_2 and ThO_2 at high temperatures, High Temp. - High Press. 15 (1983) 383–390.
[40] L. Ramond, D. Horlait, T. Delahaye, G. Jouan, A. Gauthé, B. Arab-Chapelet, S. Picart, Dilatometric study of a co-converted (U,Am)O_2 powder, J. Eur. Ceram. Soc. 36 (2016) 1775–1782.

[41] G.I. Nkou Bouala, N. Clavier, J. Lechelle, A. Mesbah, N. Dacheux, R. Podor, In situ HT-ESEM study of crystallites growth within CeO_2 microspheres, Ceram. Int. 41 (2015) 14703–14711.
[42] T.R.G. Kutty, K.B. Khan, P.V. Hegde, J. Banerjee, A.K. Sengupta, S. Majumdar, H.S. Kamath, Development of a master sintering curve for ThO_2, J. Nucl. Mater. 327 (2004) 211–219.
[43] G.I. Nkou Bouala, N. Clavier, S. Martin, J. Léchelle, J. Favrichon, H.P. Brau, N. Dacheux, R. Podor, From in Situ HT-ESEM Observations to Simulation: How Does Polycrystallinity Affects the Sintering of CeO_2 Microspheres?, J. Phys. Chem. C. 120 (2016) 386–395.
[44] D. Bernache-Assollant, Chimie-physique du frittage, Hermes Science Publications, Paris, 1993.
[45] R.D. Purohit, S. Saha, A.K. Tyagi, Combustion synthesis of 5 and 10 mol% $YO_{1.5}$ doped ThO_2 powders, J. Nucl. Mater. 323 (2003) 36–40.
[46] S.P.S. Badwal, Effect of dopant concentration on the grain boundary and volume resistivity of yttria-zirconia, J. Mater. Sci. Lett. 6 (n.d.) 1419–1421.
[47] M. Matsui, T. Soma, I. Oda, Stress-Induced Transformation and Plastic Deformation for Y_2O_3-Containing Tetragonal Zirconia Polycrystals, J. Am. Ceram. Soc. 69 (1986) 198–202.
[48] P.-L. Chen, I.-W. Chen, Role of Defect Interaction in Boundary Mobility and Cation Diffusivity of CeO_2, J. Am. Ceram. Soc. 77 (1994) 2289–2297.
[49] P.-L. Chen, I.-W. Chen, Grain Growth in CeO_2: Dopant Effects, Defect Mechanism, and Solute Drag, J. Am. Ceram. Soc. 79 (1996) 1793–1800.
[50] T. Zhang, P. Hing, H. Huang, J. Kilner, Sintering and grain growth of CoO-doped CeO_2 ceramics, J. Eur. Ceram. Soc. 22 (2002) 27–34.
[51] T.R.G. Kutty, P.V. Hegde, J. Banerjee, K.B. Khan, A.K. Sengupta, G.C. Jain, S. Majumdar, H.S. Kamath, Densification behaviour of ThO_2–PuO_2 pellets with varying PuO_2 content using dilatometry, J. Nucl. Mater. 312 (2003) 224–235.
[52] A. Pieragnoli, Influence de l'adjuvant de frittage Cr_2O_3 sur l'homogeneisation de la repartition en plutonium au sein d'une pastille MOX heterogene, PhD Thesis, Universite de Limoges, 2007.
[53] P. Balakrishna, B.P. Varma, T.S. Krishnan, T.R.R. Mohan, P. Ramakrishnan, Thorium oxide: Calcination, compaction and sintering, J. Nucl. Mater. 160 (1988) 88–94.
[54] P. Balakrishna, T.R. Ramamohan, P. Ramakrishnan, Sintering of Uranium Dioxide as a Fuel for Nucler Reactors—A Review, Trans. Indian Ceram. Soc. 46 (1987) 153–161.
[55] R. Chaim, G. Basat, A. Kats-Demyanets, Effect of oxide additives on grain growth during sintering of nanocrystalline zirconia alloys, Mater. Lett. 35 (1998) 245–250.
[56] C. Clausell, A. Barba, L. Nuño, J.C. Jarque, Effect of average grain size and sintered relative density on the imaginary part – μ″ of the complex magnetic permeability of $(Cu_{0.12}Ni_{0.23}Zn_{0.65})Fe_2O_4$ system, Ceram. Int. 42 (2016) 4256–4261.
[57] G. Bernard-Granger, C. Guizard, A. Addad, Sintering of an ultra pure α-alumina powder: I. Densification, grain growth and sintering path, J. Mater. Sci. 42 (2007) 6316–6324.
[58] M.-W. Wu, Y.-C. Chen, The Sintering Trajectory and Electrical Properties of Niobium-Doped Titania Sputtering Targets, J. Am. Ceram. Soc. 98 (2015) 163–170.
[59] D.Y. Kosyanov, P.V. Mateichenko, I.O. Vorona, R.P. Yavetskii, A.V. Tolmachev, Sintering trajectory of the 2.88 Y_2O_3-0.12 Nd_2O_3-5Al_2O_3 powders of different sizes, J. Superhard Mater. 37 (2015) 63–65.
[60] L. Chrétien, L. Bonnet, R. Boulesteix, A. Maître, C. Sallé, A. Brenier, Influence of hot isostatic pressing on sintering trajectory and optical properties of transparent Nd:YAG ceramics, J. Eur. Ceram. Soc. 36 (2016) 2035–2042.

[61] J. Kanters, U. Eisele, J. Rödel, Effect of initial grain size on sintering trajectories, Acta Mater. 48 (2000) 1239–1246.
[62] D. Bernache-Assollant, Tech. Ing. AF6620 (2005).
[63] A. Michels, C.E. Krill, H. Ehrhardt, R. Birringer, D.T. Wu, Modelling the influence of grain-size-dependent solute drag on the kinetics of grain growth in nanocrystalline materials, Acta Mater. 47 (1999) 2143–2152.
[64] S.K. Dutta, R.M. Spriggs, Grain Growth in Fully Dense ZnO, J. Am. Ceram. Soc. 53 (1970) 61–62.
[65] W.W. Mullins, J. Viñals, Scaling in linear bubble models of grain growth, Acta Metall. Mater. 41 (1993) 1359–1367.
[66] D.J. Srolovitz, M.P. Anderson, G.S. Grest, P.S. Sahni, Computer simulation of grain growth-III. Influence of a particle dispersion, Acta Metall. 32 (1984) 1429–1438.
[67] G.I. Nkou Bouala, N. Clavier, J. Léchelle, J. Monnier, C. Ricolleau, N. Dacheux, R. Podor, High-temperature electron microscopy study of ThO_2 microspheres sintering, J. Eur. Ceram. Soc. 37 (2017) 727–738.
[68] H. Matzke, Atomic mechanisms of mass transport in ceramic nuclear fuel materials, J. Chem. Soc. Faraday Trans. 86 (1990) 1243–1256.
[69] H. Matzke, Diffusion processes and surface effects in non-stoichiometric nuclear fuel oxides UO_{2+x}, and (U, Pu)$O_{2\pm x}$, J. Nucl. Mater. 114 (1983) 121–135.
[70] D. Bregiroux, F. Audubert, D. Bernache-Assollant, Densification and grain growth during solid state sintering of $LaPO_4$, Ceram. Int. 35 (2009) 1115–1120.

5. SUPPLEMENTARY MATERIAL

***Table S1** : Experimental relative densities of $Th_{0.99}Y_{0.01}O_{1.995}$ versus temperature and heating time*

Temperature (°C)	Heating time (h)	Relative dgeo (%)	Relative dpycno (%)	Closed porosity (%)	Open porosity (%)
1400	*1*	66	/	/	/
	2	77	/	/	/
	4	73	/	/	/
	8	75	/	/	/
1500	*1*	74	/	/	/
	2	78	/	/	/
	4	83	/	/	/
	8	88	/	/	/
1600	*1*	85	/	/	/
	2	90	95	5	5
	4	92	97	3	5
	8	93	97	3	4
1700	*2*	95	98	2	3
	8	98	99	1	1

***Table S2** : Experimental relative densities of $Th_{0.92}Y_{0.08}O_{1.96}$ versus temperature and heating time*

Temperature (°C)	Heating time (h)	Relative dgeo (%)	Relative dpycno (%)	Closed porosity (%)	Open porosity (%)
1400	*1*	61	/	/	/
	2	74	/	/	/
	4	71	/	/	/
	8	76	/	/	/
1500	*1*	79	/	/	/
	2	81	94	6	13
	4	83	99	1	16
	8	87	100	0	13
1600	*1*	88	100	0	12
	2	92	100	0	8
	4	96	100	0	4
	8	98	100	0	2
1700	*2*	98	100	0	2
	8	98	100	0	2

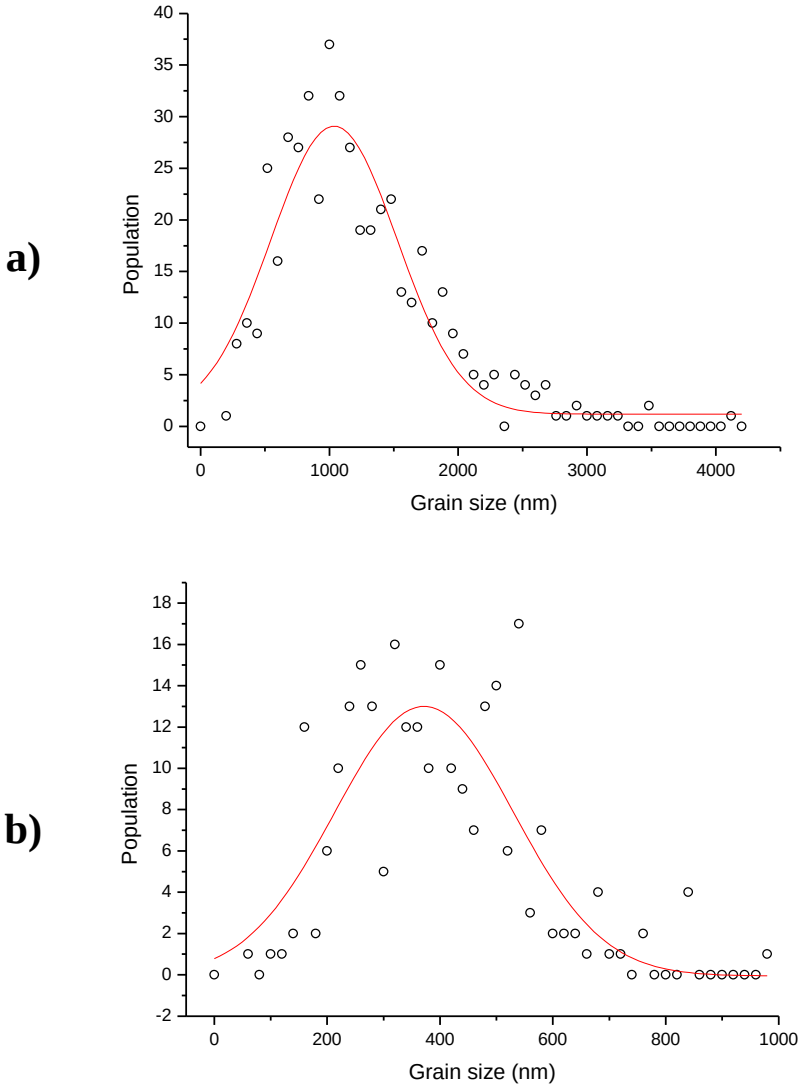

Figure S1 *: Grain size distributions of* ***(a)*** $Th_{0.99}Y_{0.01}O_{1.995}$ *and* ***(b)*** $Th_{0.85}Y_{0.15}O_{1.925}$ *sintered during 8 hours at 1600°C.*